JOURNAL OF AIRCRAFT
Vol. 43, No. 6, November–December 2006

Flight Dynamics of Highly Flexible Flying Wings

Mayuresh J. Patil*
Virginia Polytechnic Institute and State University, Blacksburg, Virginia 24061-0203
and
Dewey H. Hodges†
Georgia Institute of Technology, Atlanta, Georgia 30332-1510

DOI: 10.2514/1.17640

The paper presents a theory for flight-dynamic analysis of highly flexible flying-wing configurations. The analysis takes into account large aircraft motion coupled with geometrically nonlinear structural deformation subject only to a restriction to small strain. A large motion aerodynamic loads model is integrated into the analysis. The analysis can be used for complete aircraft analysis including trim, stability analysis linearized about the trimmed-state, and nonlinear simulation. Results are generated for a typical high-aspect-ratio "flying-wing" configuration. The results indicate that the aircraft undergoes large deformation during trim. The flight-dynamic characteristics of the deformed aircraft are completely different as compared with a rigid aircraft. When the example aircraft is loaded sufficiently, the pair of complex-conjugate short-period roots merges to become two real roots, and the phugoid mode goes unstable. Furthermore, nonlinear flight simulation of the aircraft indicates that the phugoid instability leads to catastrophic consequences.

I. Introduction

THE analysis and design of very light, and thus highly flexible, flying-wing configurations is of interest for the development of the next generation of high-altitude, long-endurance (HALE), unmanned aerial vehicles. The flexibility of such aircraft leads to large deformation, so that linear theories are not relevant for their analysis. For example, the trim shape of a large flexible aircraft is highly dependent on the flight mission (payload) as well as on the flight condition; the deformed shape is significantly different from the undeformed shape. Thus, the flight-dynamic response based on the actual trim shape can be quite different from that calculated based on linear, small deformation assumptions. In fact, the designer can use the deformation of the aircraft to positively affect the flight stability and control characteristics.

There has been limited research in the area of nonlinear aeroelasticity and flight dynamics of flying-wing configurations. Some of the earliest work was conducted by Weisshaar and Ashley [1] and was focused on static aeroelasticity of flying wings with application to oblique wing aircraft [2]. There has been recent interest in aeroelasticity and flight dynamics of flying-wing aircraft. Banerjee [3] conducted aeroelastic analysis of a tailless sailplane and compared it with a tailed airplane. The tailless configuration showed considerable decrease in flutter speed and had a dominant contribution of the rigid-body modes making it a coupled flight-dynamic/aeroelastic instability. Love et al. [4] have also presented the coupled flight-dynamic/aeroelastic instability of a swept flying-wing aircraft and showed the existence of body-freedom flutter.

The present paper describes a theoretical basis for the flight-dynamic response estimation of a highly flexible flying-wing. Various realistic design space requirements, including concentrated payload pods, multiple engines, multiple control surfaces, vertical surfaces, discrete dihedral, and continuous pretwist, are taken into account. The code based on the theoretical development presented here can be used in preliminary design as well as in control synthesis. This work is a continuation of work conducted by the authors over the past decade in the area of nonlinear aeroelasticity of conventional wing-tail configurations [5,6]. The focus of the present work is on flight dynamics of flying-wing configuration.

Presented at the International Forum on Aeroelasticity and Structural Dynamics, Munich, Germany, 28 June–2 July 2005; received 27 October 2005; revision received 24 March 2006; accepted for publication 21 April 2006.

*Assistant Professor, Department of Aerospace and Ocean Engineering. Senior Member AIAA.
†Professor, School of Aerospace Engineering. Fellow AIAA

II. Theory

The modeling of a flexible aircraft undergoing large deformation requires a geometrically-exact structural model coupled with a consistent large motion aerodynamic model. The present work is based on a flying-wing concept and is modeled structurally as a beam undergoing large displacement and rotation. The governing equations are the geometrically-exact equations of motion from Hodges [7] written in their intrinsic form (i.e., without displacement and rotational variables). However, instead of being augmented by the displacement- and rotation-based kinematical relations given therein, they are instead augmented by the intrinsic kinematical equations, derived in [8] by eliminating the displacement and rotational variables from the kinematical equations of [7]. A two-dimensional (2-D) airfoil model is appropriate for the very high-aspect-ratio wing (without fuselage interference) being analyzed here. The airloads here are based on the finite-state airloads models presented by Peters and Johnson [9].

Before presenting the structural and aerodynamic theory used for the present research, there is a need to present the supporting preliminaries, including the frames and variables. The next section presents details of the nomenclature, which are essential to understand the theoretical details presented later.

A. Preliminaries

The axis system is as shown in Fig. 1. The following frames of reference are used:

1) i is the inertial frame (z pointing in the direction of gravity).

2) b is the undeformed beam frame (x along the beam axis and y pointing towards the front of the airplane; y and z are the axes in which the cross-sectional stiffness and inertia matrices are calculated).

3) B is a deformed/moving beam cross-sectional frame.

4) a is an aerodynamic frame in which the aerodynamic lift and moment is defined (y and z are defined in the airfoil frame with z pointing perpendicular to the aerodynamic surface; y and z are the axes in which the aerodynamic coefficients are calculated).

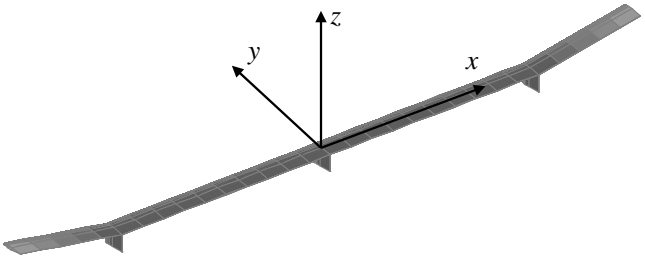

Fig. 1 Axis system for the aircraft.

The following rotation matrices are used to transform vectors in different frames:

1) $C_a = C^{ba}$ transforms a vector from the aerodynamic frame of reference to the undeformed beam cross-sectional frame of reference because the aerodynamic frame is defined relative to the structural frame, $C^{BA} = C^{ba}$, where A is the aerodynamic frame of the deformed beam.

2) $C_{\text{lr}}$is the rotation matrix at a node with a slope discontinuity that transforms variables from a reference frame on the right of the node to one on the left of the node.

3) $C = C^{Bb}$ determines the deformed beam cross-sectional frame of reference. For the intrinsic formulation presented here, C is not required to solve the equations but may be used in postprocessing.

The following primary beam variables are column matrices containing the measure numbers of the indicated vectors in the deformed beam cross-sectional frame B:

1) F contains internal force measures in the B-frame.
2) M contains the internal moment measures in the B-frame.
3) Ω contains the angular velocity measures in the B-frame.
4) V contains the velocity measures in the B-frame.
5) g contains the measure numbers of the gravity vector in the B-frame.

The following secondary beam variables are column matrices of the indicated vectors, expressed in the bases of the indicated frames:

1) γ contains force strain measures in the B-frame.
2) κ contains moment strain measures in the B-frame.
3) P contains the linear momentum measures in the B-frame.
4) H contains the angular momentum measures in the B-frame.

B. Structural Model

The geometrically-exact, intrinsic equations for the dynamics of a general, nonuniform, twisted, curved, anisotropic beam, undergoing large deformation, are given as

$$F' + (\tilde{k} + \tilde{\kappa})F + f = \dot{P} + \tilde{\Omega}P \tag{1}$$

$$M' + (\tilde{k} + \tilde{\kappa})M + (\tilde{e}_1 + \tilde{\gamma})F + m = \dot{H} + \tilde{\Omega}H + \tilde{V}P \tag{2}$$

$$V' + (\tilde{k} + \tilde{\kappa})V + (\tilde{e}_1 + \tilde{\gamma})\Omega = \dot{\gamma} \tag{3}$$

$$\Omega' + (\tilde{k} + \tilde{\kappa})\Omega = \dot{\kappa} \tag{4}$$

where $k = \lfloor k_1 k_2 k_3 \rfloor$ is the initial twist/curvature of the beam, $e_1 = \lfloor 1\ 0\ 0 \rfloor^T$, and f and m are the external forces including gravity (f_g, m_g), aerodynamic loads ($f_{\text{aero}}, m_{\text{aero}}$), and thrust ($f_T, m_T$). The first two equations in the preceding set are the equations of motion [7], whereas the latter two are the intrinsic kinematical equations [8] derived from the generalized strain-displacement and generalized velocity-displacement equations.

1. Cross-Sectional Constitutive Laws

The secondary beam variables are linearly related to the primary variables by the cross-sectional constitutive laws (flexibility and inertia matrices), such that

$$\begin{Bmatrix} \gamma \\ \kappa \end{Bmatrix} = \begin{bmatrix} R & S \\ S^T & T \end{bmatrix} \begin{Bmatrix} F \\ M \end{Bmatrix} \tag{5}$$

$$\begin{Bmatrix} P \\ H \end{Bmatrix} = \begin{bmatrix} \mu\Delta & -\mu\tilde{\xi} \\ \mu\tilde{\xi} & I \end{bmatrix} \begin{Bmatrix} V \\ \Omega \end{Bmatrix} \tag{6}$$

where R, S, and T are 3×3 matrices of cross-sectional flexibility coefficients, and μ, ξ, and I are the mass per unit length, mass center offset, and mass moment of inertia per unit length, respectively. These relations are derived based on the assumptions of small strain and slenderness.

2. Finite-Element Discretization

To solve the above set of equations, the beam is discretized into finite elements. The equations for each element are obtained by discretizing the differential equations such that energy is conserved [8]. For example, consider a variable X. Let the nodal values of the variable after discretization be represented by $\hat{X}_l^n$ and $\hat{X}_r^n$, where the superscript denotes the node number, the subscript denotes the left or right side of the node, and the hat denotes that it is nodal value. The need to define two values of the variable at a node is clarified in a later section. For the element n

$$X' = \frac{\hat{X}_l^{n+1} - \hat{X}_r^n}{dl} \tag{7}$$

$$X = \bar{X}^n = \frac{\hat{X}_l^{n+1} + \hat{X}_r^n}{2} \tag{8}$$

In a discretized form the equations of motion can be written as

$$\frac{\hat{F}_l^{n+1} - \hat{F}_r^n}{dl} + (\widetilde{\bar{\kappa}^n} + \widetilde{\bar{k}^n})\bar{F}^n + \bar{f}^n - \dot{\bar{P}}^n - \widetilde{\bar{\Omega}^n}\bar{P}^n = 0 \tag{9}$$

$$\frac{\hat{M}_l^{n+1} - \hat{M}_r^n}{dl} + (\widetilde{\bar{\kappa}^n} + \widetilde{\bar{k}^n})\bar{M}^n + (\tilde{e}_1 + \widetilde{\bar{\gamma}^n})\bar{F}^n + \bar{m}^n - \dot{\bar{H}}^n - \widetilde{\bar{\Omega}^n}\bar{H}^n - \widetilde{\bar{V}^n}\bar{P}^n = 0 \tag{10}$$

$$\frac{\hat{V}_l^{n+1} - \hat{V}_r^n}{dl} + (\widetilde{\bar{\kappa}^n} + \widetilde{\bar{k}^n})\bar{V}^n + (\tilde{e}_1 + \widetilde{\bar{\gamma}^n})\bar{\Omega}^n - \dot{\bar{\gamma}}^n = 0 \tag{11}$$

$$\frac{\hat{\Omega}_l^{n+1} - \hat{\Omega}_r^n}{dl} + (\widetilde{\bar{\kappa}^n} + \widetilde{\bar{k}^n})\bar{\Omega}^n - \dot{\bar{\kappa}}^n = 0 \tag{12}$$

where, as defined in the preceding section, the barred quantities correspond to the values of the variables in the element interior whereas the hatted quantities are nodal values. The barred and hatted quantities of the primary variables are related as

$$\bar{F}^n = \frac{\hat{F}_l^{n+1} + \hat{F}_r^n}{2} \tag{13}$$

$$\bar{M}^n = \frac{\hat{M}_l^{n+1} + \hat{M}_r^n}{2} \tag{14}$$

$$\bar{V}^n = \frac{\hat{V}_l^{n+1} + \hat{V}_r^n}{2} \tag{15}$$

$$\bar{\Omega}^n = \frac{\hat{\Omega}_l^{n+1} + \hat{\Omega}_r^n}{2} \tag{16}$$

The barred secondary variables are related to the barred primary variables as stated above in the cross-sectional constitutive law.

3. Gravity Loads

The force term in the equations of motion includes gravitational forces. The gravitational force and moment are

$$f_g = \mu g \tag{17}$$

$$m_g = \mu \tilde{\xi} g \tag{18}$$

where g is a column matrix of the measure numbers of the gravity vector expressed in the B basis.

The measure numbers of the gravity vector are known in the i-frame. Its measure numbers in the B-frame at all the nodes can be calculated using the following equations:

$$g' + (\tilde{\kappa} + \tilde{k})g = 0 \qquad \dot{g} + \tilde{\Omega} g = 0 \tag{19}$$

which in the discretized form can be written as

$$\frac{\hat{g}_l^{n+1} - \hat{g}_r^n}{dl} + (\widetilde{\bar{\kappa}^n} + \widetilde{\bar{k}^n})\bar{g}^n = 0 \qquad \dot{\hat{g}} + \tilde{\hat{\Omega}}\,\hat{g} = 0 \tag{20}$$

Equation (20), the time-differentiated equation, is satisfied at one node, whereas Eq. (19), the spatially-differentiated one, is used to obtain g at other nodes. Both equations are matrix equations, i.e., a set of three scalar equations. In both cases, the three equations together can be shown to satisfy a constraint of constant magnitude for g. One can thus replace any one of the three dynamic equations by the static form of this length constraint. This will remove the artificial root caused by the differentiation of a constraint. Also, the constraint is satisfied for the steady-state calculation when the dynamic terms are neglected, and so the equation can be written as

$$(e_1 e_1^T + e_2 e_2^T)\dot{\hat{g}}^{n_g} + (e_1 e_1^T + e_2 e_2^T)\widetilde{\hat{\Omega}^{n_g}}\hat{g}^{n_g} + (e_3 e_3^T)|\hat{g}^{n_g}| = e_3 \tag{21}$$

For the case of symmetric flight at the central node, $\hat{\Omega}_2 = \hat{\Omega}_3 = 0$. Thus, the above equations become

$$\dot{\hat{g}}_1 = 0 \quad \Rightarrow \quad \hat{g}_1 = 0 \tag{22}$$

$$\dot{\hat{g}}_2 - \hat{\Omega}_1 \hat{g}_3 = 0 \tag{23}$$

$$(\hat{g}_2)^2 + (\hat{g}_3)^2 = 1 \tag{24}$$

From Eq. (23), it is clear that for steady-state, symmetric flight, $\hat{\Omega}_1 = 0$ because $\hat{g}_3 \neq 0$; $\hat{g}_3 = 0$ when the wing is vertical (e.g., 90 deg bank) though it is also possible for 90 deg pitch or a combination of both.

4. Engines, Nodal Masses, Vertical Surfaces, and Slope Discontinuities

Because of nodal mass, nodal force (thrust), and slope discontinuities, the force on one side of the node is different from the force on the other side of the node. Thus,

$$\hat{F}_r^n - \hat{C}_{lr}^{n^T}\hat{F}_l^n + \hat{f}_T^n + \hat{\mu}^n \hat{g}_r^n + \hat{f}_{\text{aero}}^n - \dot{\hat{P}}_r^n - \widetilde{\hat{\Omega}_r^n}\hat{P}_r^n = 0 \tag{25}$$

$$\hat{M}_r^n - \hat{C}_{lr}^{n^T}\hat{M}_l^n + \hat{m}_T^n + \hat{\mu}^n \widetilde{\hat{\xi}^n}\hat{g}_r^n + \hat{m}_{\text{aero}}^n - \dot{\hat{H}}_r^n - \widetilde{\hat{\Omega}_r^n}\hat{H}_r^n - \widetilde{\hat{V}_r^n}\hat{P}_r^n = 0 \tag{26}$$

where $\hat{f}_T^n$ is the discrete nodal thrust force defined in the $()_r$ reference frame, $\hat{m}_T^n$ is the corresponding nodal moment, $\hat{\mu}^n$ is the concentrated nodal mass, $\hat{\xi}^n$ is the corresponding mass offset, $\hat{f}_{\text{aero}}^n$ and $\hat{m}_{\text{aero}}^n$ are the aerodynamic forces due to vertical surfaces/pods, and $\hat{P}_r^n$ and $\hat{H}_r^n$ are the linear and angular momenta of the concentrated modal mass, given by

$$\begin{Bmatrix} \hat{P}_r^n \\ \hat{H}_r^n \end{Bmatrix} = \begin{bmatrix} \hat{\mu}^n \Delta & -\hat{\mu}^n \widetilde{\hat{\xi}^n} \\ \hat{\mu}^n \widetilde{\hat{\xi}^n} & \hat{I}^n \end{bmatrix} \begin{Bmatrix} \hat{V}_r^n \\ \hat{\Omega}_r^n \end{Bmatrix} + \begin{Bmatrix} 0 \\ \hat{H}_{\text{engine}}^n \end{Bmatrix} \tag{27}$$

where $\hat{I}^n$ is the mass moment of inertia matrix of the concentrated mass and $\hat{H}_{\text{engine}}^n$ is the angular momentum of the engine.

A slope discontinuity in the beam will also change all the other variables, such that

$$\hat{V}_l^n = \hat{C}_{lr}^n \hat{V}_r^n \tag{28}$$

$$\hat{\Omega}_l^n = \hat{C}_{lr}^n \hat{\Omega}_r^n \tag{29}$$

$$\hat{g}_l^n = \hat{C}_{lr}^n \hat{g}_r^n \tag{30}$$

The $()_r$ variables can be used to replace $()_l$ variables for V, Ω, and g, thus reducing the number of variables.

5. Final Structural Equations

The preceding development leads to the following primary equations:

$$\hat{F}_r^n - \hat{C}_{lr}^{n^T}\hat{F}_l^n + \hat{f}_T^n + \hat{\mu}^n \hat{g}_r^n + \hat{f}_{\text{aero}}^n - \dot{\hat{P}}_r^n - \widetilde{\hat{\Omega}_r^n}\hat{P}_r^n = 0 \tag{31}$$

$$\hat{M}_r^n - \hat{C}_{lr}^{n^T}\hat{M}_l^n + \hat{m}_T^n + \hat{\mu}^n \widetilde{\hat{\xi}^n}\hat{g}_r^n + \hat{m}_{\text{aero}}^n - \dot{\hat{H}}_r^n - \widetilde{\hat{\Omega}_r^n}\hat{H}_r^n - \widetilde{\hat{V}_r^n}\hat{P}_r^n = 0 \tag{32}$$

$$\frac{\hat{F}_l^{n+1} - \hat{F}_r^n}{dl} + (\widetilde{\bar{\kappa}^n} + \widetilde{\bar{k}^n})\bar{F}^n + \bar{f}_{\text{aero}}^n + \mu^n \bar{g}^n - \dot{\bar{P}}^n - \widetilde{\bar{\Omega}^n}\bar{P}^n = 0 \tag{33}$$

$$\frac{\hat{M}_l^{n+1} - \hat{M}_r^n}{dl} + (\widetilde{\bar{\kappa}^n} + \widetilde{\bar{k}^n})\bar{M}^n + (\tilde{e}_1 + \widetilde{\bar{\gamma}^n})\bar{F}^n + \bar{m}_{\text{aero}}^n + \mu^n \tilde{\bar{\xi}}^n \bar{g}^n - \dot{\bar{H}}^n - \widetilde{\bar{\Omega}^n}\bar{H}^n - \widetilde{\bar{V}^n}\bar{P}^n = 0 \tag{34}$$

$$\frac{\hat{C}_{lr}^{n+1}\hat{V}_r^{n+1} - \hat{V}_r^n}{dl} + (\widetilde{\bar{\kappa}^n} + \widetilde{\bar{k}^n})\bar{V}^n + (\tilde{e}_1 + \widetilde{\bar{\gamma}^n})\bar{\Omega}^n - \dot{\bar{\gamma}}^n = 0 \tag{35}$$

$$\frac{\hat{C}_{lr}^{n+1}\hat{\Omega}_r^{n+1} - \hat{\Omega}_r^n}{dl} + (\widetilde{\bar{\kappa}^n} + \widetilde{\bar{k}^n})\bar{\Omega}^n - \dot{\bar{\kappa}}^n = 0 \tag{36}$$

$$\frac{\hat{C}_{lr}^{n+1}\hat{g}_r^{n+1} - \hat{g}_r^n}{dl} + (\widetilde{\bar{\kappa}^n} + \widetilde{\bar{k}^n})\bar{g}^n = 0 \tag{37}$$

and, the following secondary equations

$$\begin{Bmatrix} \bar{\gamma}^n \\ \bar{\kappa}^n \end{Bmatrix} = \begin{bmatrix} R^n & S^n \\ S^{n^T} & T^n \end{bmatrix} \begin{Bmatrix} \bar{F}^n \\ \bar{M}^n \end{Bmatrix} \tag{38}$$

$$\begin{Bmatrix} \bar{P}^n \\ \bar{H}^n \end{Bmatrix} = \begin{bmatrix} \mu^n \Delta & -\mu^n \widetilde{\bar{\xi}^n} \\ \mu^n \widetilde{\bar{\xi}^n} & I^n \end{bmatrix} \begin{Bmatrix} \bar{V}^n \\ \bar{\Omega}^n \end{Bmatrix} \tag{39}$$

$$\bar{F}^n = \frac{\hat{F}_l^{n+1} + \hat{F}_r^n}{2} \tag{40}$$

$$\bar{M}^n = \frac{\hat{M}_l^{n+1} + \hat{M}_r^n}{2} \tag{41}$$

$$\bar{V}^n = \frac{\hat{C}_{lr}^{n+1}\hat{V}_r^{n+1} + \hat{V}_r^n}{2} \tag{42}$$

$$\bar{\Omega}^{n} = \frac{\hat{C}_{lr}^{n+1}\hat{\Omega}_{r}^{n+1} + \hat{\Omega}_{r}^{n}}{2} \tag{43}$$

$$\bar{g}^{n} = \frac{\hat{C}_{lr}^{n+1}\hat{g}_{r}^{n+1} + \hat{g}_{r}^{n}}{2} \tag{44}$$

$$\begin{Bmatrix} \hat{P}_{r}^{n} \\ \hat{H}_{r}^{n} \end{Bmatrix} = \begin{bmatrix} \hat{\mu}^{n}\Delta & -\hat{\mu}^{n}\widetilde{\hat{\xi}^{n}} \\ \hat{\mu}^{n}\widetilde{\hat{\xi}^{n}} & \hat{I}^{n} \end{bmatrix} \begin{Bmatrix} \hat{V}_{r}^{n} \\ \hat{\Omega}_{r}^{n} \end{Bmatrix} + \begin{Bmatrix} 0 \\ \hat{H}_{\text{engine}}^{n} \end{Bmatrix} \tag{45}$$

6. Boundary Conditions

The following are the boundary conditions for the complete aircraft problem:

$$\hat{F}_{l}^{1} = 0 \tag{46}$$

$$\hat{M}_{l}^{1} = 0 \tag{47}$$

$$\hat{F}_{r}^{N+1} = 0 \tag{48}$$

$$\hat{M}_{r}^{N+1} = 0 \tag{49}$$

$$(e_1e_1^T + e_2e_2^T)\dot{\hat{g}}^{n_g} + (e_1e_1^T + e_2e_2^T)\widetilde{\hat{\Omega}^{n_g}}\hat{g}^{n_g} + (e_3e_3^T)|\hat{g}^{n_g}| = 0 \tag{50}$$

where N denotes the total number of elements and n_g denotes the reference node for gravity.

C. Aerodynamic Model

1. Lift, Drag, and Pitching Moment Expressions

The airloads are calculated based on 2-D aerodynamics using known airfoil parameters.

First the velocities in the aerodynamic frame at the midchord are written as

$$\bar{V}_{a}^{n} = C_{a}^{n^T}\bar{V}^{n} - \tilde{y}_{\text{mc}}^{n}C_{a}^{n^T}\bar{\Omega}^{n} \tag{51}$$

$$\bar{\Omega}_{a}^{n} = C_{a}^{n^T}\bar{\Omega}^{n} \tag{52}$$

where y_{mc}^{n} is a row matrix containing the measures of the position vector from the beam reference axis to the midchord and can be written in terms of the aerodynamic center (at the quarter-chord) location as $y_{\text{mc}}^{n} = \lfloor 0\ \bar{y}_{\text{ac}}^{n} - (b^n/2)\ 0 \rfloor$.

The lift, drag, and pitching moment at the quarter-chord are given by:

$$L_{\text{aero}}^{n} = \rho b^{n} V_{T}^{n^2}(C_{l_0}^{n} + C_{l_\alpha}^{n}\sin\alpha^{n} + C_{l_\beta}^{n}\beta^{n}) + \rho b^{n} V_{T}^{n} V_{a_2}^{n} C_{l_\alpha}^{n}\alpha_{\text{rot}}^{n}\cos\alpha^{n} \tag{53}$$

$$D_{\text{aero}}^{n} = \rho b^{n} V_{T}^{n^2} C_{d_0}^{n} + \rho b^{n} V_{T}^{n} V_{a_2}^{n} C_{l_\alpha}^{n}\alpha_{\text{rot}}^{n}\sin\alpha^{n} \tag{54}$$

$$M_{\text{aero}}^{n} = 2\rho b^{n^2} V_{T}^{n^2}(C_{m_0}^{n} + C_{m_\alpha}^{n}\sin\alpha^{n} + C_{m_\beta}^{n}\beta^{n}) - \rho b^{n^2} V_{T}^{n} V_{a_2}^{n} C_{l_\alpha}^{n}\alpha_{\text{rot}}^{n}/2 \tag{55}$$

where

$$V_{T}^{n} = \sqrt{V_{a_2}^{n^2} + V_{a_3}^{n^2}} \tag{56}$$

$$\sin\alpha^{n} = \frac{-V_{a_3}^{n}}{V_{T}^{n}} \tag{57}$$

$$\alpha_{\text{rot}}^{n} = \frac{\Omega_{a_1}^{n} b^{n}/2}{V_{T}^{n}} \tag{58}$$

and $V_{a_2}^{n}$ and $V_{a_3}^{n}$ are the measure numbers of $\bar{V}_{a}^{n}$. β^{n} is the flap deflection of the nth element.

The lift, drag, and pitching moment are the aerodynamic loads to be applied to the wing and can be written in the a-frame as:

$$f_{a}^{n} = \begin{Bmatrix} 0 \\ -L_{\text{aero}}^{n}\frac{V_{a_3}^{n}}{V_{T}^{n}} - D_{\text{aero}}^{n}\frac{V_{a_2}^{n}}{V_{T}^{n}} \\ L_{\text{aero}}^{n}\frac{V_{a_2}^{n}}{V_{T}^{n}} - D_{\text{aero}}^{n}\frac{V_{a_3}^{n}}{V_{T}^{n}} \end{Bmatrix} \tag{59}$$

$$m_{a}^{n} = \begin{Bmatrix} M_{\text{aero}}^{n} \\ 0 \\ 0 \end{Bmatrix} \tag{60}$$

Finally, the aerodynamic forces derived above are transformed to the B-frame and transferred to the beam reference axis to give the applied aerodynamic forces as

$$\bar{f}_{\text{aero}}^{n} = C_{a}^{n} f_{a}^{n} \tag{61}$$

$$\overline{m}_{\text{aero}}^{n} = C_{a}^{n} m_{a}^{n} + C_{a}^{n}\tilde{y}_{\text{ac}}^{n} f_{a}^{n} \tag{62}$$

2. Unsteady Effects

The above aerodynamic model is a quasi-steady one with neither wake (inflow) effects nor apparent mass effects. To add those effects into the model we have to first add the inflow λ_0 and acceleration terms in the force and moment equation. Secondly, we have to include an inflow model that calculates λ_0. Here, the Peters 2-D inflow theory [10] is used.

The force and moment expressions with the unsteady aerodynamics effects are

$$f_{a}^{n} = \rho b^{n}\begin{Bmatrix} 0 \\ -(C_{l_0}^{n} + C_{l_\beta}^{n}\beta^{n})V_{T}^{n}V_{a_3}^{n} + C_{l_\alpha}^{n}(V_{a_3}^{n} + \lambda_{0}^{n})^2 - C_{d_0}^{n}V_{T}^{n}V_{a_2}^{n} \\ (C_{l_0}^{n} + C_{l_\beta}^{n}\beta^{n})V_{T}^{n}V_{a_2}^{n} - C_{l_\alpha}^{n}\dot{V}_{a_3}^{n} b/2 - C_{l_\alpha}^{n}V_{a_2}^{n}(V_{a_3}^{n} + \lambda_{0}^{n} - \Omega_{a_1}^{n} b^{n}/2) - C_{d_0}^{n}V_{T}^{n}V_{a_3}^{n} \end{Bmatrix} \tag{63}$$

and

$$m_{a}^{n} = 2\rho b^{n^2}\begin{Bmatrix} (C_{m_0}^{n} + C_{m_\beta}^{n}\beta^{n})V_{T}^{n^2} - C_{m_\alpha}^{n}V_{T}^{n}V_{a_3}^{n} - b^{n}C_{l_\alpha}^{n}/8V_{a_2}^{n}\Omega_{a_1}^{n} - b^{n^2}C_{l_\alpha}^{n}\dot{\Omega}_{a_1}^{n}/32 + b^{n}C_{l_\alpha}^{n}\dot{V}_{a_3}^{n}/8 \\ 0 \\ 0 \end{Bmatrix} \tag{64}$$

The inflow model can be written as

$$[A_{\text{inflow}}]\{\dot{\lambda}^n\} + \left(\frac{V_T^n}{b^n}\right)\{\lambda^n\} = \left(-\dot{V}_{a_3}^n + \frac{b^n}{2}\dot{\Omega}_{a_1}^n\right)\{c_{\text{inflow}}\} \quad (65)$$

and

$$\lambda_0^n = \frac{1}{2}\{b_{\text{inflow}}\}^T\{\lambda^n\} \quad (66)$$

where λ^n is a column matrix of inflow states for the nth element, and $[A_{\text{inflow}}]$, $\{c_{\text{inflow}}\}$, $\{b_{\text{inflow}}\}$ are constant matrices derived in [10].

D. Aeroelastic System

An aeroelastic model is obtained by coupling the aerodynamic force definition given in the previous section with the set of equations presented in the section on the structural model. The aeroelastic equations are nonlinear equations in terms of the primary variables (F_l^n, F_r^n, M_l^n, M_r^n, V_r^n, Ω_r^n, and g_r^n).

The set of aeroelastic equations is solved using the Newton–Raphson method to obtain the steady-state (trim) solution. The Jacobian calculated for this solution is needed to assess the stability of the linearized system at the trim state.

E. Trimming

The trim conditions are the same as steady-state conditions, i.e., all the time-derivatives are zero. If all the controls are given, then the solution gives the steady-state (trim) corresponding to that flight condition. On the other hand, more often it is desired to trim the flight at a specific trim state. To do so, the trim state in terms of the airspeed and flight angle (climb/descent indicator) are prescribed and the controls (thrust and flap angle) are determined. Thus, two additional equations and two variables (controls) are appended to the system. The two equations are given below. The equations are sufficient for a symmetric trimmed state of flight. For asymmetric trimmed flight, the equations would be modified and additional equations relating the radius of turn and side-slip would be added. The symmetric trim equations are

$$\hat{g}_2\hat{V}_2 + \hat{g}_3\hat{V}_3 - \tan\phi(\hat{g}_3\hat{V}_2 - \hat{g}_2\hat{V}_3) = 0 \quad (67)$$

$$\hat{V}_2^2 + \hat{V}_3^2 - V_\infty^2 = 0 \quad (68)$$

where ϕ is the prescribed flight angle and V_∞ is the prescribed airspeed. The first equation is derived from the fact that $\phi = \theta - \alpha$, where θ is the pitch angle ($\tan\theta = \hat{g}_2/\hat{g}_3$) and α is the angle of attack ($\tan\alpha = -\hat{V}_3/\hat{V}_2$).

F. Post-Processing and Graphics

The solution for the intrinsic equations described above can be used to determine and plot the deformation. The following equations relate the strains and curvatures to displacements and rotations:

$$r_i' = C^{ib}e_1 \quad (69)$$

$$(C^{bi})' = -\tilde{k}C^{bi} \quad (70)$$

$$(r_i + u_i)' = C^{iB}(\gamma + e_1) \quad (71)$$

$$(C^{Bi})' = -(\tilde{\kappa} + \tilde{k})C^{Bi} \quad (72)$$

where r_i is a column matrix containing the measure numbers of the position vector of the beam axis from the origin of the reference frame i, and u_i represents the displacement expressed in the i-frame basis. The first two equations determine the geometry of the undeformed wing. The undeformed beam axis could be plotted if r_i is known at all the nodal locations, whereas the deformed beam axis could be plotted if $r_i + u_i$ is known.

To plot the wing surface, one needs the position of points on the wing surface from the beam axis. For plotting, it is assumed that the cross section is rigid, the undeformed and deformed surface can be generated by plotting $r_i + C^{ib}\zeta$ and $r_i + u_i + C^{iB}\zeta$, respectively, where ζ represents the cross-sectional position vector.

The discretized strain-displacement equations are

$$\hat{C}^{bi^{n+1}} = \left(\frac{\Delta}{dl} + \frac{\tilde{k}^n}{2}\right)^{-1}\left(\frac{\Delta}{dl} - \frac{\tilde{k}^n}{2}\right)\hat{C}^{bi^n} \quad (73)$$

$$r_i^{n+1} = r_i^n + \bar{C}^{ib^n}e_1 dl \quad (74)$$

$$\hat{C}^{Bi^{n+1}} = \left(\frac{\Delta}{dl} + \frac{\tilde{\bar{\kappa}}^n + \tilde{k}^n}{2}\right)^{-1}\left(\frac{\Delta}{dl} - \frac{\tilde{\bar{\kappa}}^n + \tilde{k}^n}{2}\right)\hat{C}^{Bi^n} \quad (75)$$

$$r_i^{n+1} + u_i^{n+1} = r_i^n + u_i^n + \bar{C}^{iB^n}(\bar{\gamma}^n + e_1)dl \quad (76)$$

G. Validation

The present analysis has been implemented in a program called nonlinear aeroelastic trim and stability for HALE aircraft (NATASHA). This program has been validated using various reference results. The validation studies include convergence of structural frequencies and modeshapes of prismatic beams with a number of finite elements, convergence of nonlinear steady-state and linearized frequencies of a rotating prismatic beam, various buckling loads including Euler buckling and lateral-torsional buckling, various flutter speeds due to follower forces including Beck flutter and lateral-torsional flutter, and the divergence, reversal, and flutter speeds of the Goland wing as well as a HALE wing used in our prior research.

III. Example

Consider the aircraft as illustrated in Fig. 2. The example aircraft has a span of 238.78 ft and a constant chord of 8 ft. One-sixth of the span at each end has a dihedral of 10 deg. The inertial, elastic, and aerodynamic properties of the wing cross section are given in Table 1.

There are five propulsive units; one at the midspan and two each at one-third and two-thirds semispan distance from the midspan. There are three vertical surfaces (pods) which act as the landing gear. Two of the pods weigh 50 lb each and are located at two-thirds semispan distance from the midspan. The central pod also acts as a bay for payload and weighs between 60 lb ("empty") and 560 lb ("full"). The pod/payload weight is assumed to a be a point mass hanging 3 ft under the wing. The aerodynamic coefficients for the pods are $C_{l_\alpha} = 5$ and $C_{d_0} = 0.02$.

A. Trim Results

NATASHA begins a flight-dynamic analysis of flexible aircraft with a trim analysis. The trim solution involves the steady-state solution of the complete nonlinear equations. For a symmetric aircraft, one could calculate the trim solution (the airspeed and rate of climb) at a specified thrust and flap deflection. Here, we use a trimming algorithm to calculate the thrust (assumed constant for each of the five motors) and flap deflection (assumed constant throughout

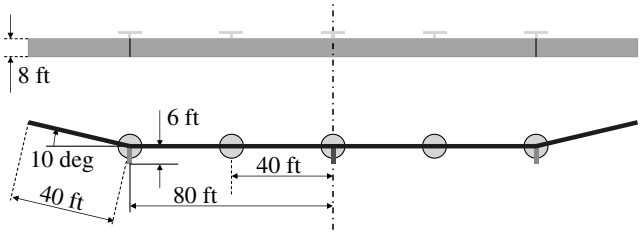

Fig. 2 Geometry of the aircraft.

Table 1 Wing cross-sectional properties

Structural properties (values)	
Elastic (reference) axis	25% chord
Torsional rigidity	0.4×10^6 lb ft^2
Bending rigidity	2.5×10^6 lb ft^2
Bending rigidity (chordwise)	30×10^6 lb ft^2
Mass per unit length	6 lb/ft
Center of gravity	25% chord
Centroidal mass moments of inertia (values)	
About x-axis (torsional)	30 lb ft
About y-axis	5 lb ft
About z-axis	25 lb ft
Aerodynamic coefficients at 25% chord (values)	
C_{l_α}	2π
C_{l_δ}	1
C_{d_0}	0.01
C_{m_0}	0.025
C_{m_δ}	−0.25

the span) to achieve a specified trim state. For most of the results in this paper, the trim solution is calculated for a level flight condition of 40 ft/s at sea level. Figure 3 shows the control values, the flight angle of attack, and the structural deformation as a function of the payload weight for the aircraft. The results for a rigid aircraft with the same configuration are also shown.

Figure 3d shows the trim shape of the aircraft. The given aircraft, for the empty configuration, has an almost evenly distributed mass (gravitational forces) balanced by aerodynamic forces and thus the equivalent loads and deformation of the aircraft are small. With the addition of the concentrated payload at the center we get significantly higher aerodynamic loads. Such loads lead to large deformation in the highly flexible aircraft. The "U" shape of the full configuration has very different structural, as well as flight-dynamic, characteristics as will be seen throughout the rest of the paper.

Figure 3a shows the thrust required for the specified trim condition. The change in required thrust is insignificant for payload changes because the primary source of drag for such aircraft is the profile drag and the skin-friction drag. This drag does not change with the aircraft weight. The induced drag which is proportional to the lift (and thus aircraft gross weight) is minor for very high-aspect-ratio aircraft.

The flap deflection required for trim is shown in Fig. 3b. The flap deflection is used for pitch control of the aircraft. As the aircraft deforms to a U-shape, the center of gravity position moves forward relative the aerodynamic center and thus lower flap deflection is required to provide the pitch-down moment

The (root) angle of attack at the trim condition is shown in Fig. 3c. The angle of attack increases with payload as expected. The difference in the rigid and flexible angle of attack comes from two sources, the aeroelastic deformation and the direction of the lift. The aircraft in its undeformed shape has negligible aeroelastic coupling since the aerodynamic center and the shear center are coincident. But as the aircraft deforms, the drag on the wings leads to nose-up twisting moment at the root, in turn leading to aeroelastic deformation. Thus, lower root angle of attack is sufficient to provide the required lift. On the other hand, the lift generated is perpendicular to the airfoil, and, as the deformation increases, the direction in which the lift acts departs more and more from the vertical. Thus, for large deformation, because the aerodynamic vertical force is reduced, a larger angle of attack is required to generate the same amount of vertical force.

B. Linear Longitudinal Stability Estimation

The aircraft as a flight-dynamic/aeroelastic system is nonlinear. Once the nonlinear trim is calculated, NATASHA can then simulate the aircraft flight for various control settings and/or external disturbances using the complete nonlinear equations. In addition, it is prudent to gauge the response of the system by investigating the dynamics of small perturbation motions of the aircraft about its trimmed state by using equations that are linearized about that state. By analyzing this linearized system, we can gauge the stability as well as the response for small disturbances. Here, the focus is on analyzing the longitudinal flight dynamics of the aircraft in detail.

The linear symmetric flight dynamics performance of the aircraft is normally discussed in terms of the phugoid and short-period modes of the aircraft. The two modes are the only symmetric modes of a rigid aircraft. It should be noted that the flexible aircraft has a large number of modes which have flexible as well as aircraft motion. For most conventional aircraft, one would still be able to separate the modes into two flight-dynamic modes which are dominated by aircraft motion and the rest as flexible modes dominated by structural deformation. For the present aircraft, the low frequency flexible

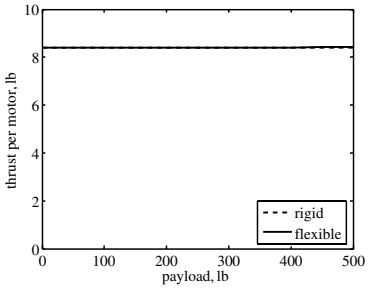

a) Trim thrust per motor required for specified trim

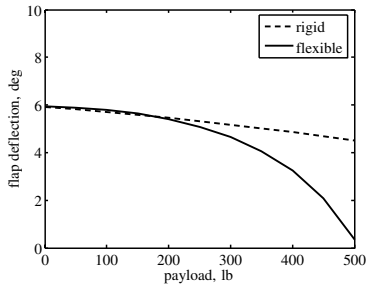

b) Trim flap deflection required for specified trim

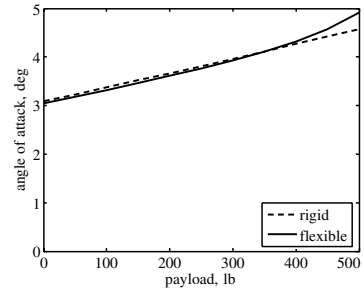

c) Trim angle of attack at the trim condition

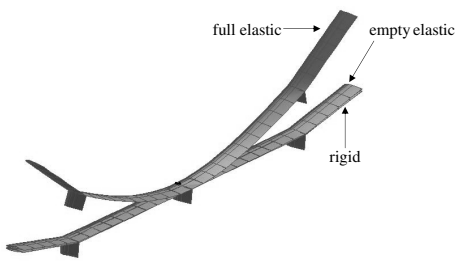

d) Elastic deformation of the aircraft at trim

Fig. 3 Trim results for a rigid as well as flexible aircraft as a function of payload at 40 ft/s, sea level.

Table 2 Flight dynamics roots

		Empty payload	Full payload
Rigid model	phugoid	$-0.106 \pm 0.146i$	$-0.0613 \pm 0.535i$
	short period	$-2.84 \pm 1.82i$	$-3.05 \pm 1.63i$
Flexible model	phugoid	$-0.108 \pm 0.142i$	$+0.147 \pm 0.586i$
	short period	$-2.74 \pm 1.76i$	——

modes of the aircraft are in the same frequency range as the flight-dynamic modes and thus there is strong coupling between the modes.

Table 2 presents the short-period and phugoid modes for the rigid and flexible aircraft at the empty and full payload configuration. The frequency of the phugoid mode increases in frequency while the damping decreases with added payload mass. For the flexible aircraft, the damping crosses the imaginary axis and the mode becomes unstable for payloads above 260 lb. The root locus of the phugoid mode for the range of payload mass is shown in Fig. 4a.

The short-period mode root locus is shown in Fig. 4b. The short-period mode for the rigid aircraft does not change significantly with payload. The flexible aircraft model shows a drastic change in eigenvalues of the short-period mode. The root moves rapidly with added mass, and for payloads above 95 lb, the pair of complex-conjugate short-period roots merges to become two real roots. This can be expected because, for increase in payload, there is a corresponding increase in the deformation. The deformed U-shape leads to an order-of-magnitude increase in the pitch moment of inertia, and thus there is corresponding decrease in the frequency. Therefore, this highly flexible aircraft does not show a classical short-period mode in its deformed state when it is loaded sufficiently.

The phugoid mode of the aircraft can lead to instability and is thus investigated in detail. Figure 5 shows the unstable phugoid mode shape for the full configuration. The phugoid mode shows the classical coupling of pitch and airspeed. The expected exchange of kinetic and potential energy is also seen in Fig. 5b. The aircraft loses potential energy as it loses altitude but gains kinetic energy (airfoils are further apart). In the present case, the strain energy due to deformation is also involved. As seen from Fig. 5d, the elastic deformation is significant, but it is not the dominant factor in the motion of the aircraft. The mode can be clearly seen by observing

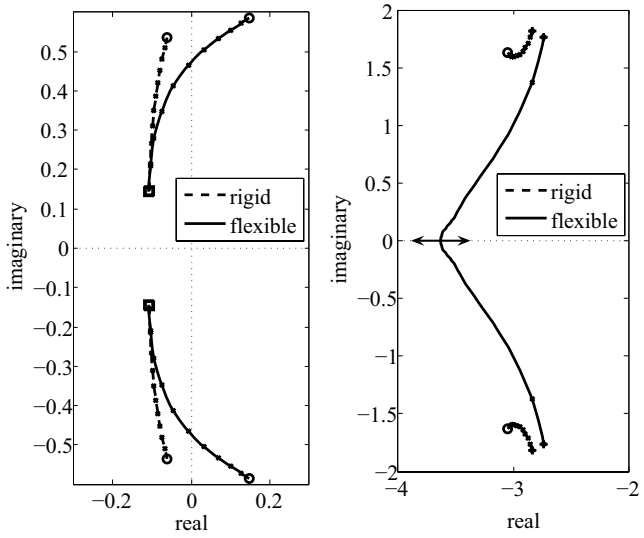

a) Phugoid mode **b) Short-period mode**

Fig. 4 Root locus for a rigid as well as flexible aircraft as a function of payload; the trim condition is 40 ft/s at sea level (square represents empty configuration whereas circle represents full).

a) Inertial 3-D view of the aircraft (aircraft moving to the left)

b) Inertial 2-D view of the midspan section (aircraft moving to the left)

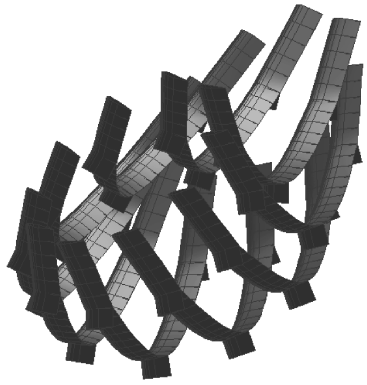

c) 3-D view of the aircraft for an observer moving at trim airspeed (aircraft motion is clockwise)

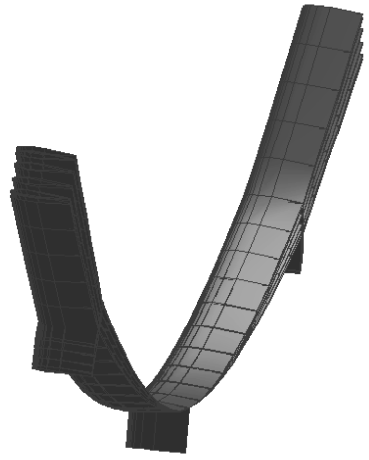

d) Elastic deformation of the aircraft

Fig. 5 Phugoid mode of the flexible configuration with 500 lb payload.

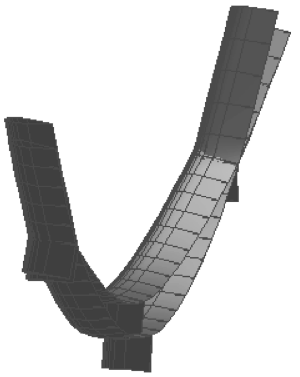

a) First bending (dominant); $-2.8583 \pm 2.1057i$

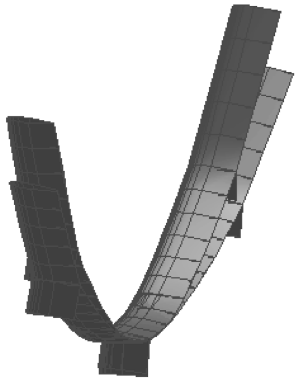

b) Coupled bending, torsion, aircraft plunge; $-3.6045 \pm 2.9881i$

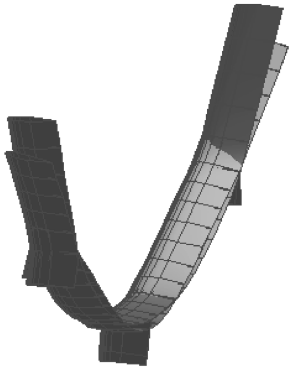

c) Second bending (dominant); $-2.0735 \pm 5.1086i$

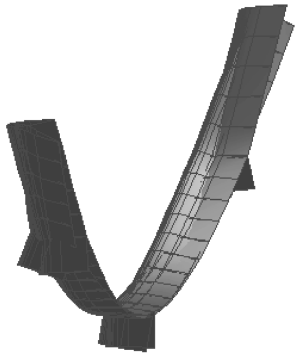

d) Coupled bending, torsion, aircraft pitch; $-1.3762 \pm 6.3915i$

Fig. 6 Flexible modes of the aircraft.

Fig. 5c. Here, the aircraft motion due to trimmed flight is removed so as to focus on the perturbations about the trimmed flight condition. The figure shows the classical elliptical motion of the aircraft about its expected trim position.

Figure 6 shows the four flexible modes with the lowest eigenvalues. Though some of these modes can be said to be dominant in bending, the others are coupled modes with torsion, bending (both directions), and aircraft motion (pitch and plunge). In fact, one of the modes develops from the real eigenvalue of the short-period mode.

C. Nonlinear Simulation

Linear stability analysis estimates the response of the system to small disturbances. Linear analysis does not provide information regarding response to large excitation or the response of an unstable system. To estimate the large deformation response of the system we have to solve the complete dynamic nonlinear equations in time. NATASHA uses a simple, second-order, central-difference, time marching algorithm with high frequency damping.

Figure 7 shows the nonlinear response of full aircraft at 40 ft/s. The aircraft simulation is initiated at the trim state. An external disturbance is introduced by adding a flap deflection. A maximum 5 deg flap deflection is added to trim flap deflection. The shape of the excitation is a ramp up between 1 and 2 s, and a ramp down between 2 and 3 s. After 3 s, the flap deflection is maintained at the trim value. A time step of 0.02 s is used for the simulation. The simulations for a time step of 0.01 s as well as 0.05 s are practically the same.

As expected, the unstable phugoid mode gets excited and the amplitude of oscillation increases. The exchange of potential and kinetic energy is seen in Fig. 7a. Within 2–3 cycles of the oscillations, the aircraft starts experiencing very high angles of attack at the highest altitudes. Because stall is not modeled in the simulation, the results after stall do not represent the real aircraft motion. The motion of the aircraft is visualized in Fig. 7b. It is obvious from this figure

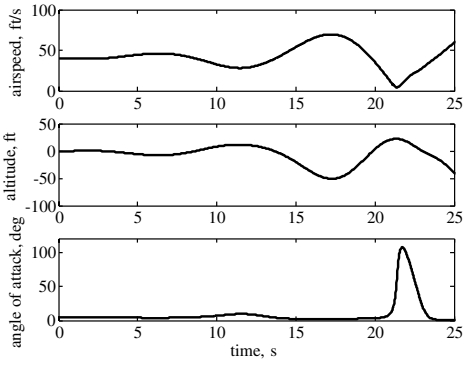

a) Variation in aircraft parameters

b) Inertial 2-D view of the midspan section, time 0–25 s (aircraft moving to the left)

c) Inertial 2-D view of the midspan section, time 25–50 s (showing pitch loops)

Fig. 7 Nonlinear simulation of aircraft response to initial flap excitation.

that once dynamic stall is modeled one would see a slightly different response at the highest altitudes.

NATASHA is robust enough to run for all possible large aircraft motion as long as the strain is small. If the simulation is run for a longer time, then one sees the aircraft perform pitch loops (Fig. 7c). During the pitch loops, however, the angle of attack stays small, and stall is not expected. As expected from an unstable mode [11], there is loss of energy for a constant thrust and aircraft loses altitude. Again, the results after the aircraft experiences stall cannot be trusted as the present theory does not include a stall model.

IV. Conclusion

A complete theoretical methodology for the analysis of a highly flexible flying wing has been presented. The analysis methodology is based on geometrically-exact beam theory for elastic deformation coupled with large motion airfoil aerodynamic theory. The rigid-body degrees of freedom are accounted by including the gravity vector in the formulation. The equations for the complete analysis, including trim, linear stability, and nonlinear simulation are "intrinsic", i.e., the equations do not require displacement and rotation variables. The analysis accounts for realistic design space requirements including concentrated payload pods, multiple engines, multiple control surfaces, vertical surfaces, discrete dihedral, and continuous pretwist.

An example of a typical, flexible, flying-wing aircraft is presented and analyzed. The aircraft is very flexible and undergoes large deformation for full payload configuration because the payload is concentrated at the center (rather than being evenly distributed over the wing). The trim shape and the corresponding trim control requirements are calculated using a trim algorithm. The trim shape as expected is a U-shape. Because of the change in the shape, the flight-dynamic modes, as well as the flexible modes, change significantly. When the example aircraft is loaded sufficiently, the pair of complex-conjugate short-period roots merges to become two real roots, so that the classical short-period mode does not exist at trim because of the large pitch moment of inertia of the deformed configuration. The classical phugoid mode becomes unstable with increase in payload (trim aircraft deformation). Nonlinear simulation of the aircraft confirms that the unstable phugoid mode can be catastrophic for such aircraft.

References

[1] Weisshaar, T. A., and Ashley, H., "Static Aeroelasticity and the Flying Wing," *Journal of Aircraft*, Vol. 10, No. 10, 1973, pp. 586–594.

[2] Wintzer, M., Sturdza, P., and Kroo, I., "Conceptual Design of Conventional and Oblique Wing Configurations for Small Supersonic Aircraft," *44th AIAA Aerospace Sciences Meeting and Exhibit*, AIAA Paper 2006-930, 2006.

[3] Banerjee, J. R., "Flutter Characteristics of High Aspect Ratio Tailless Aircraft," *Journal of Aircraft*, Vol. 21, No. 9, 1984, pp. 733–736.

[4] Love, M., Zink, P., Wieselmann, P., and Youngren, H., "Body Freedom Flutter of High Aspect Ratio Flying Wings," *47th AIAA/ASME/ASCE/AHS/ASC Structures, Structural Dynamics and Materials Conference*, AIAA Paper 2005-1947, 2005.

[5] Patil, M. J., Hodges, D. H., and Cesnik, C. E. S., "Nonlinear Aeroelastic Analysis of Complete Aircraft in Subsonic Flow," *Journal of Aircraft*, Vol. 37, No. 5, Sept.–Oct. 2000, pp. 753–760.

[6] Patil, M. J., and Hodges, D. H., "On the Importance of Aerodynamic and Structural Geometrical Nonlinearities in Aeroelastic Behavior of High-Aspect-Ratio Wings," *Journal of Fluids and Structures*, Vol. 19, No. 7, Aug. 2004, pp. 905–915.

[7] Hodges, D. H., "A Mixed Variational Formulation Based on Exact Intrinsic Equations for Dynamics of Moving Beams," *International Journal of Solids and Structures*, Vol. 26, No. 11, 1990, pp. 1253–1273.

[8] Hodges, D. H., "Geometrically Exact, Intrinsic Theory for Dynamics of Curved and Twisted Anisotropic Beams," *AIAA Journal*, Vol. 41, No. 6, 2003, pp. 1131–1137.

[9] Peters, D. A., and Johnson, M. J., "Finite-State Airloads for Deformable Airfoils on Fixed and Rotating Wings," *Symposium on Aeroelasticity and Fluid/Structure Interaction, Proceedings of the Winter Annual Meeting*, American Society of Mechanical Engineers, Fairfield, NJ, Vol. 44, 1994, pp. 1–28.

[10] Peters, D. A., Karunamoorthy, S., and Cao, W.-M., "Finite State Induced Flow Models, Part 1: Two-Dimensional Thin Airfoil," *Journal of Aircraft*, Vol. 32, No. 2, March–April 1995, pp. 313–322.

[11] Patil, M. J., "From Fluttering Wings to Flapping Flight: the Energy Connection," *Journal of Aircraft*, Vol. 40, March 2003, pp. 270–276.